Supplementary Information

Atomically resolved imaging of radiation-sensitive metal-organic frameworks via electron ptychography

Guanxing Li, Ming Xu, Wen-Qi Tang, Ying Liu, Cailing Chen, Daliang Zhang, Lingmei Liu, Shoucong Ning*, Hui Zhang*, Zhi-Yuan Gu, Zhiping Lai, David A. Muller, and Yu Han*

Emails of corresponding authors:
ningustc@ustc.edu.cn
huizhang2023@scut.edu.cn
hanyu@scut.edu.cn

This PDF file includes:

1. Supplementary Figure 1 to Figure 12
2. Supplementary Table 1 and Table 2
3. Description of the Supplementary PDB File

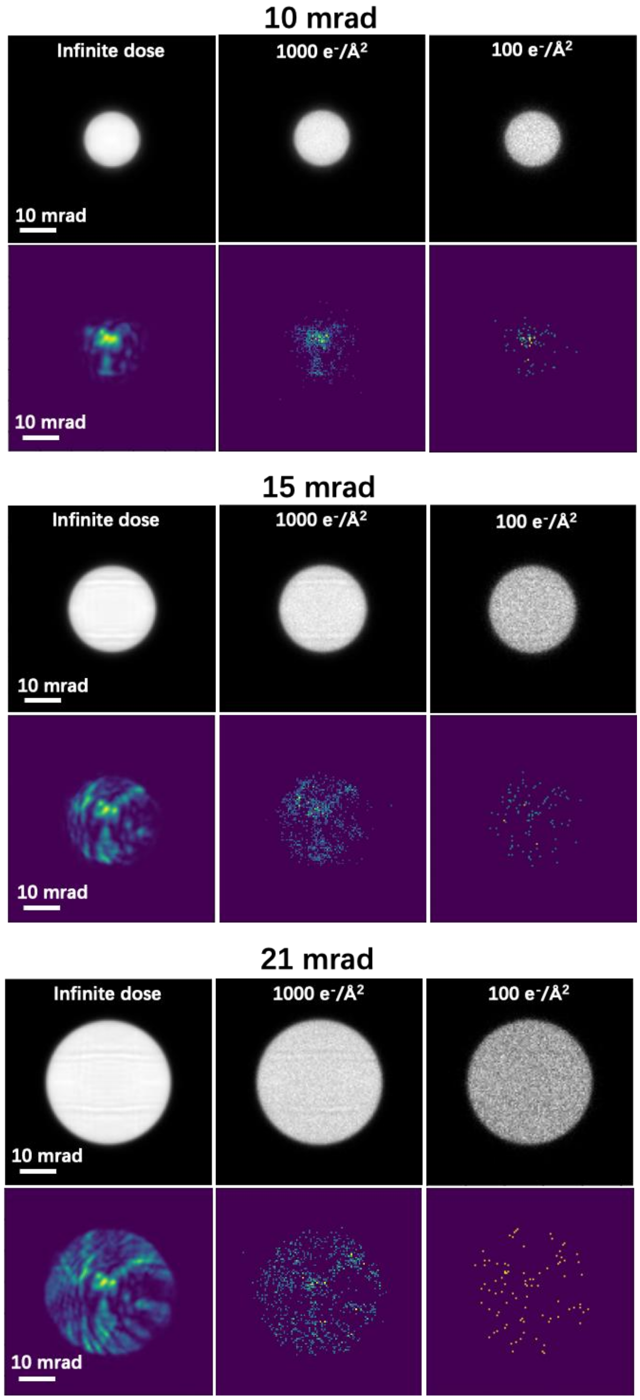

Supplementary Fig. 1. 4D-STEM data for MOF Zr-BTB simulated with varying convergence semi-angles and electron doses, as indicated. Each panel features position-averaged convergent beam electron diffraction (PACBED) patterns in the upper row and single convergent beam electron diffraction (CBED) patterns in the lower row.

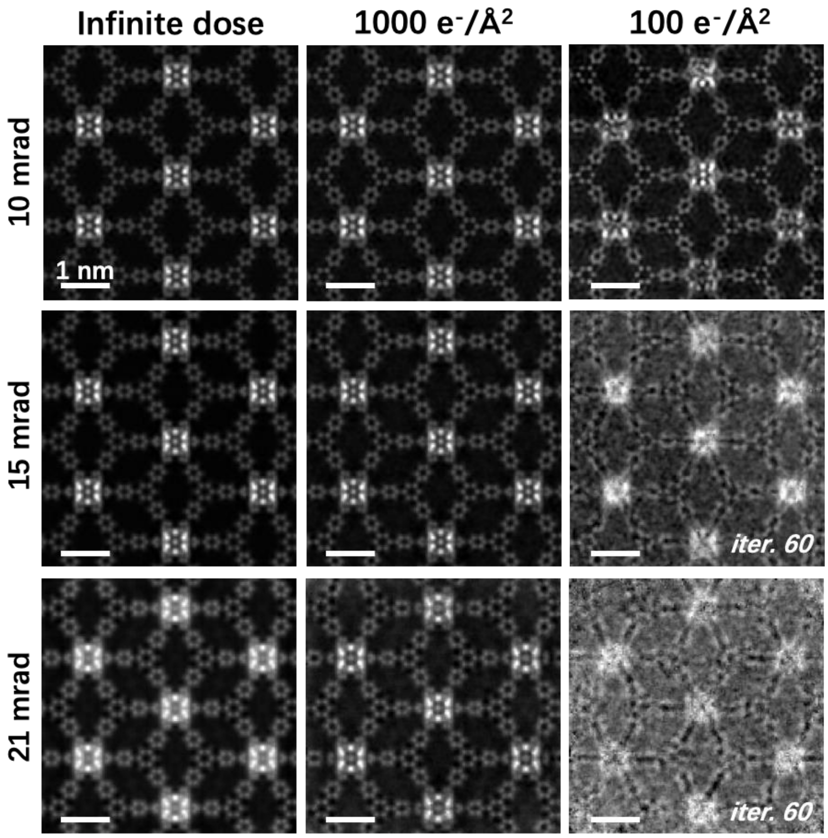

Supplementary Fig. 2. Reconstructed ptychography images of MOF Zr-BTB using 4D-STEM datasets simulated under various conditions, as indicated. The images were reconstructed using the LSQ-ML algorithm, which incorporates multislice and mixed-state methods. Ptychography images were typically generated after 200 iteration cycles, except for those labeled ‘iter. 60’. This label indicates that these images resulted from only 60 iteration cycles, after which the iterative processes failed to converge and subsequently crashed.

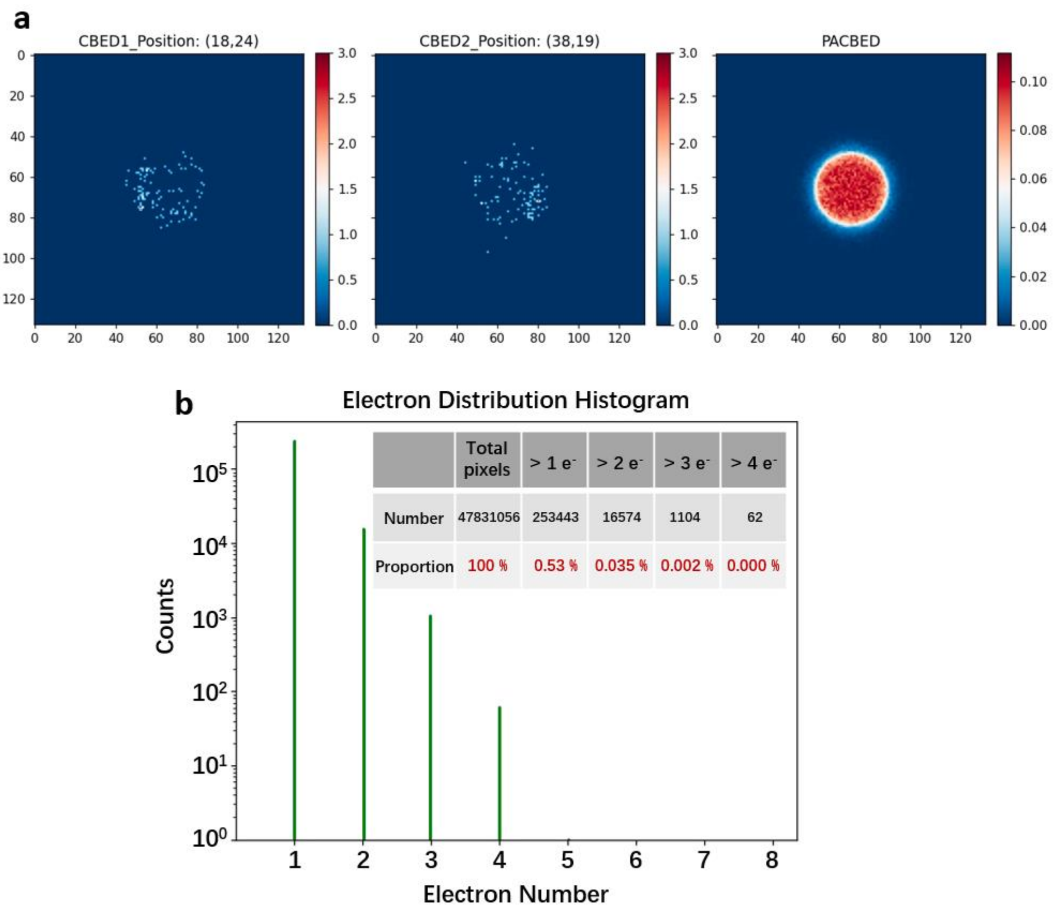

Supplementary Fig. 3. Analysis of 4D-STEM data of MOF Zr-BTB simulated under specific conditions: 10 mrad convergence semi-angle, 60 nm defocus, and a total electron dose of 100 $e^-/Å^2$. **(a)** Two representative individual CBED patterns alongside a PACBED pattern. **(b)** Histogram of electron distribution of the entire dataset.

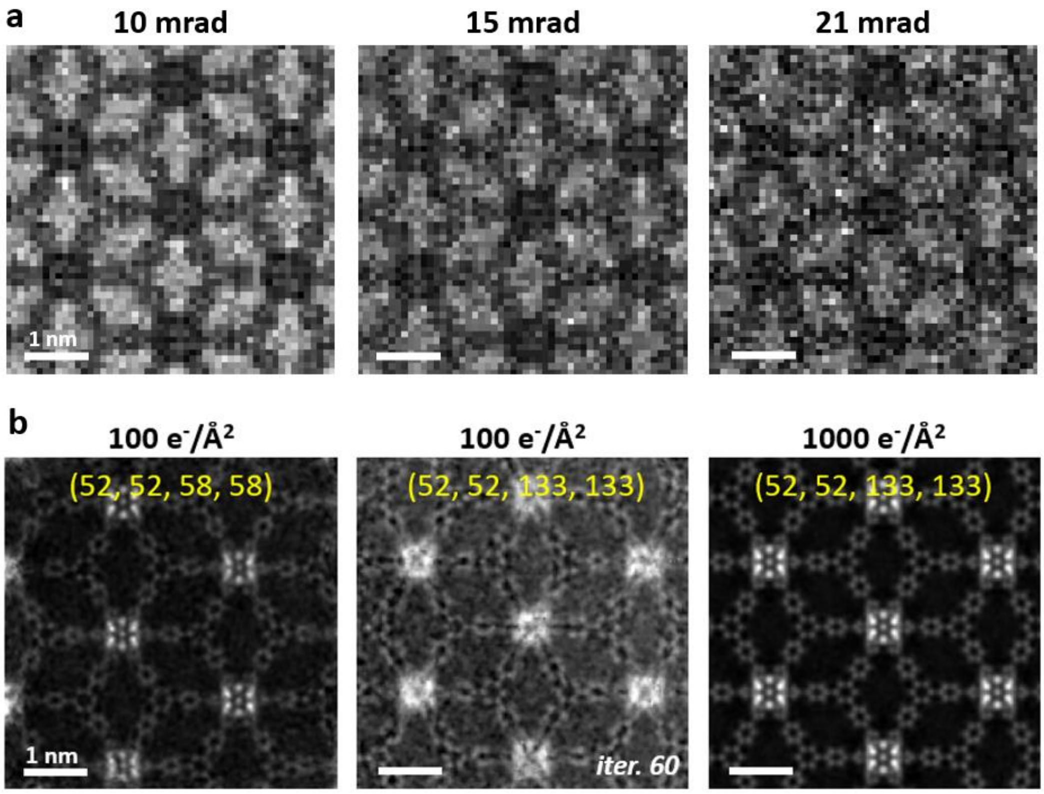

Supplementary Fig. 4. (a) Bright-field (BF)-STEM images summed from the same angular range (0-5 mrad) from datasets simulated with varying convergence semi-angles at a constant dose level of 100 $e^{-}/Å^{2}$. **(b)** Illustration of the effects of electrons/K_pixel on ptychographic reconstruction, using datasets simulated at 15 mrad.

Note: In (**a**), the signal-to-noise ratio of the BF-STEM images summed from the same angular range decreases with increasing the convergence semi-angle, demonstrating that a larger α value would allocate more signal to the high spatial frequency realm, at the expense of low frequencies. In (**b**), iterative ptychography reconstruction fails when low dose (100 $e^{-}/Å^{2}$) is coupled with a large number of K_pixels (133×133) (middle panel). This issue can be solved by either reducing the number of K_pixels (left panel) or increasing the eletron dose (right panel), further confirming that the electrons per K_pixel play a crucial role in low-dose iterative ptychography.

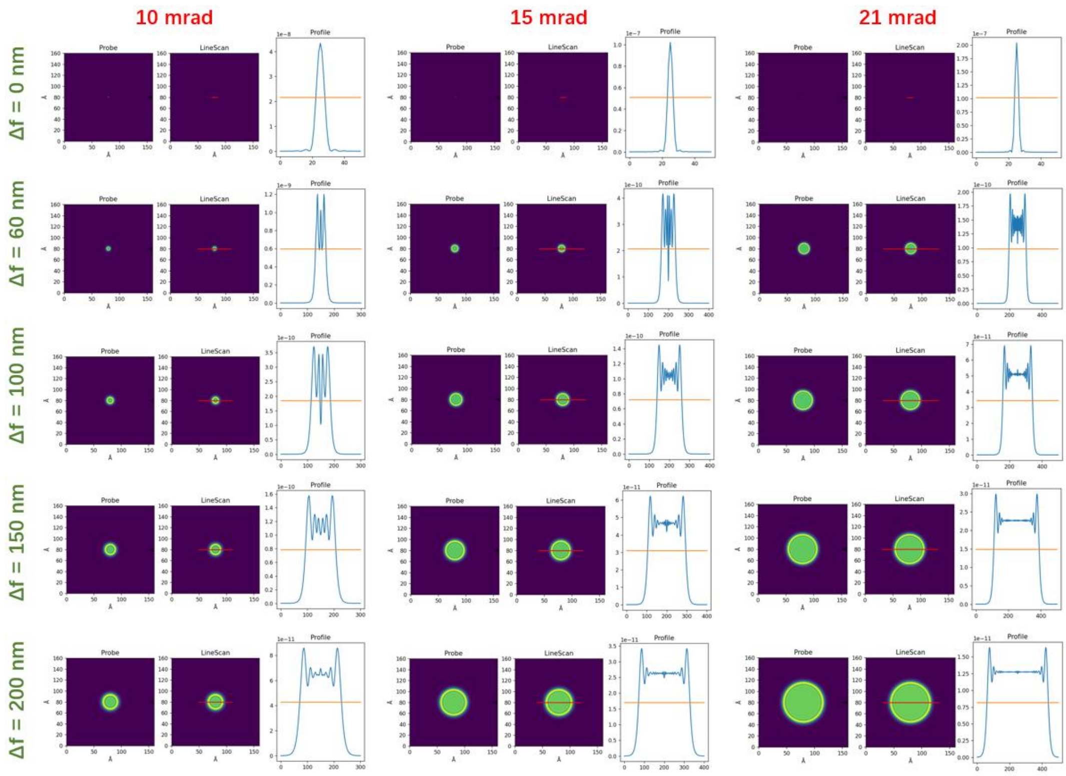

Supplementary Fig. 5. Impact of convergence semi-angle and defocus on the probe size, with other aberrations set to zero. Probe sizes are derived from the full width at half maximum of intensity profiles along the probe diameter, detailed in Supplementary Table 1.

Supplementary Table 1 Probe sizes calculated under different conditions.

300 kV					
α \ Δf	Δf = 0 nm	Δf = 60 nm	Δf = 100 nm	Δf = 150 nm	Δf = 200 nm
10 mrad	0.112 nm	0.783 nm	1.453 nm	2.295 nm	3.146 nm
15 mrad	0.072 nm	1.412 nm	2.468 nm	3.804 nm	5.158 nm
21 mrad	0.053 nm	2.140 nm	3.672 nm	5.616 nm	7.568 nm

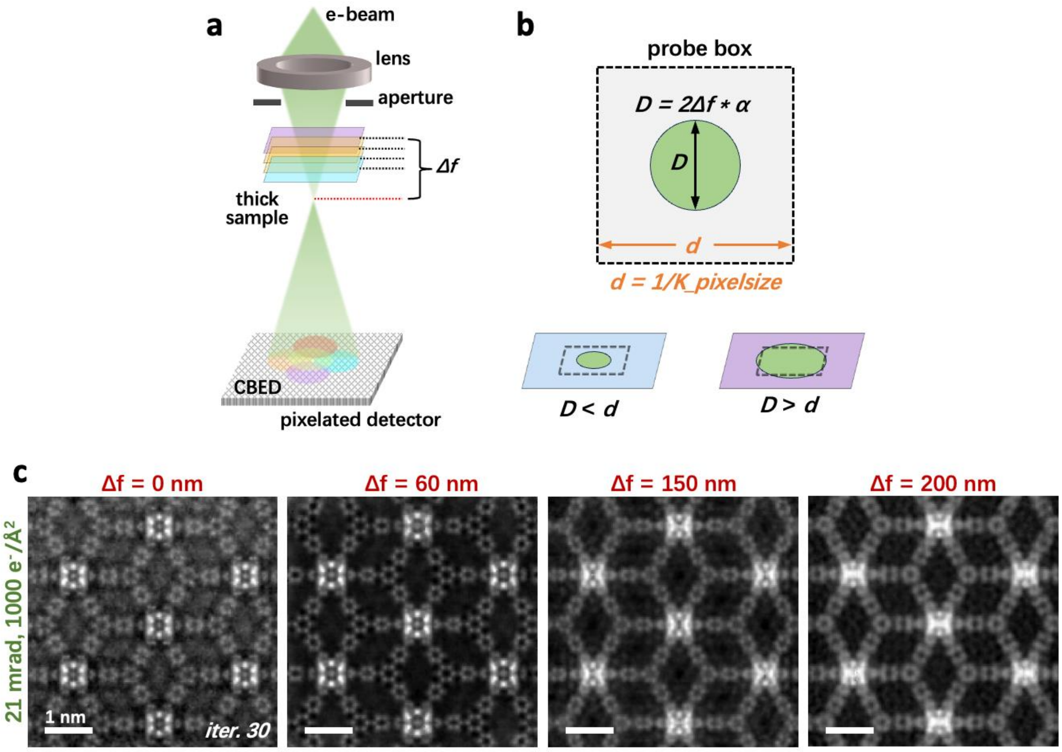

Supplementary Fig. 6. (a) Schematic illustration of 4D-STEM ptychography conducted on a thick specimen**. (b)** Relationships between probe size and probe box size. **(c)** Ptychography images of Zr-BTB reconstructed from the 4D-STEM datasets simulated at different focus values, with the convergence semi-angle and electron dose fixed at 21 mrad and 1000 $e^{-}/Å^{2}$, respectively.

Note: The top and bottom layers of a thick specimen may experience different probe sizes, as illustrated in (**a**). Particularly with large convergence semi-angle and defocus settings, it is possible for the probe size at certain depths within the specimen to exceed the reconstructed box size (e.g., the purple area in **a** and **b**). Such unfavorable situation can cause artifacts in the reconstructed images, as illustrated in (**c**), where images deviate from the projected electrostatic potential under large defocus conditions (i.e., 150 nm and 200 nm).

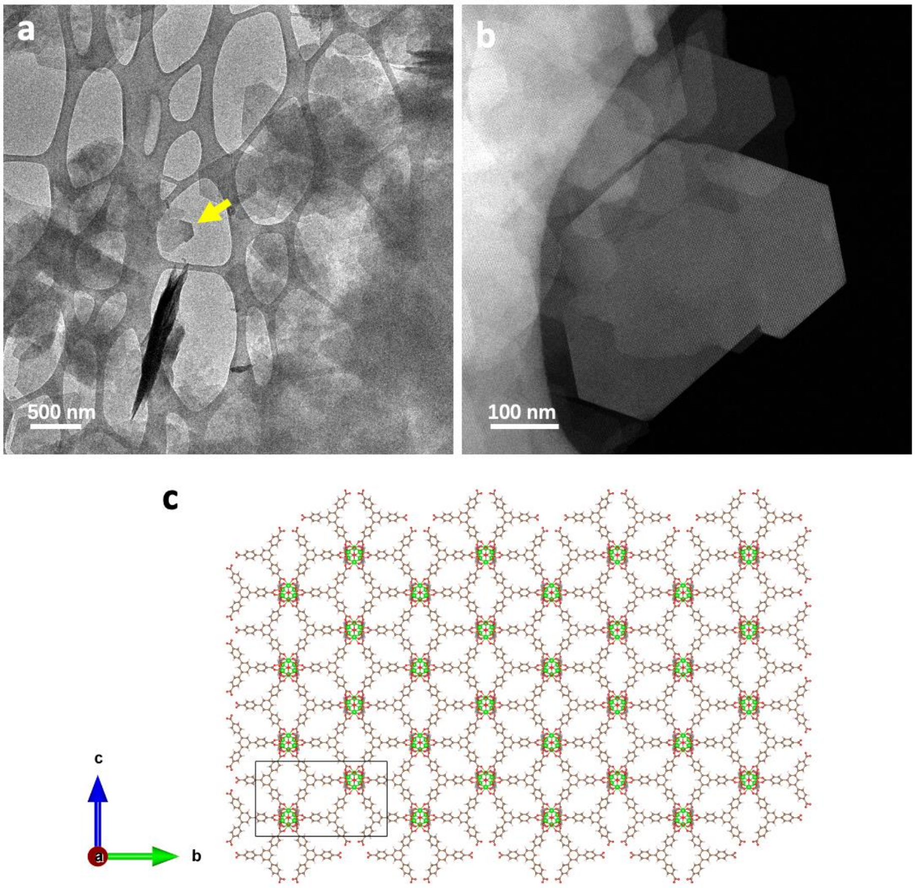

Supplementary Fig. 7. (a) Low-magnification TEM image and **(b)** HAADF-STEM image of MOF Zr-BTB crystals used for acquiring the 4D-STEM datasets. **(c)** Structural model of MOF Zr-BTB viewed along the [100] zone axis.

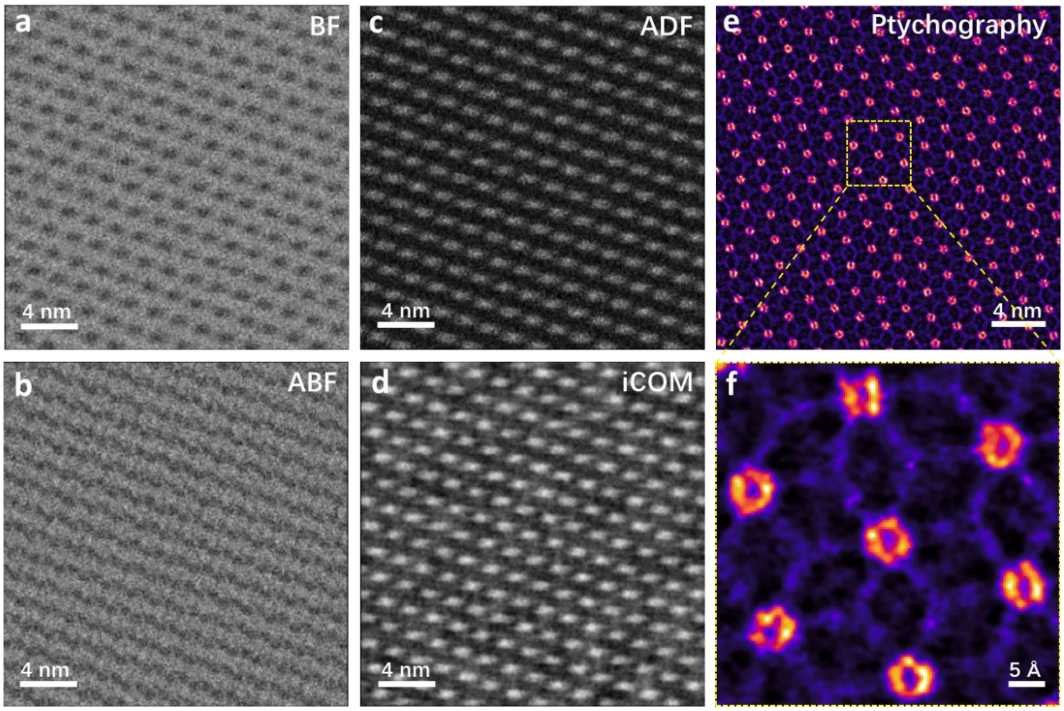

Supplementary Fig. 8. Comparison of images derived from the same 4D-STEM dataset for Zr-BTB using various imaging mechanisms: **(a)** Bright-field (BF), **(b)** annular bright-field (ABF), **(c)** annular dark-field (ADF), **(d)** integrated center-of-mass (iCOM), and **(e)** LSQ-ML-based ptychography. **(f)** Enlarged view of the square-marked area in (**e**).

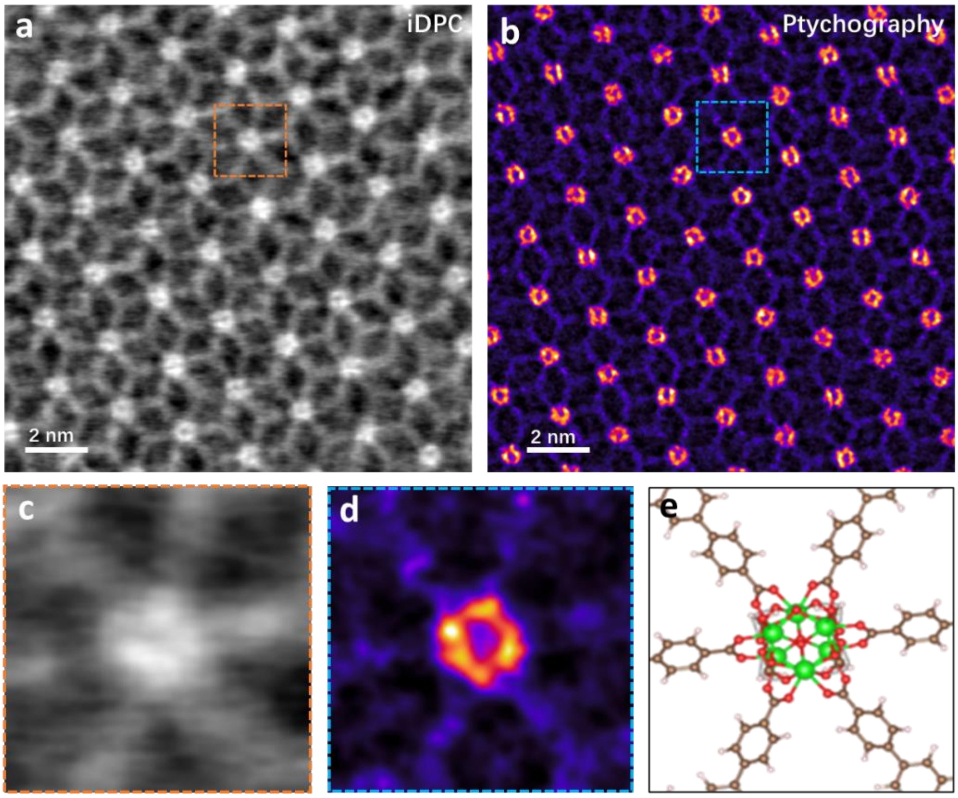

Supplementary Fig. 9. Comparisons between iDPC-STEM and 4D-STEM ptychography for imaging MOF Zr-BTB: **(a)** iDPC-STEM; **(b)** 4D-STEM ptychography. **(c)** and **(d)** show enlarged views of the marked regions in (**a**) and (**b**), respectively. (**e**) Structural model of Zr-BTB, corresponding to the marked region.

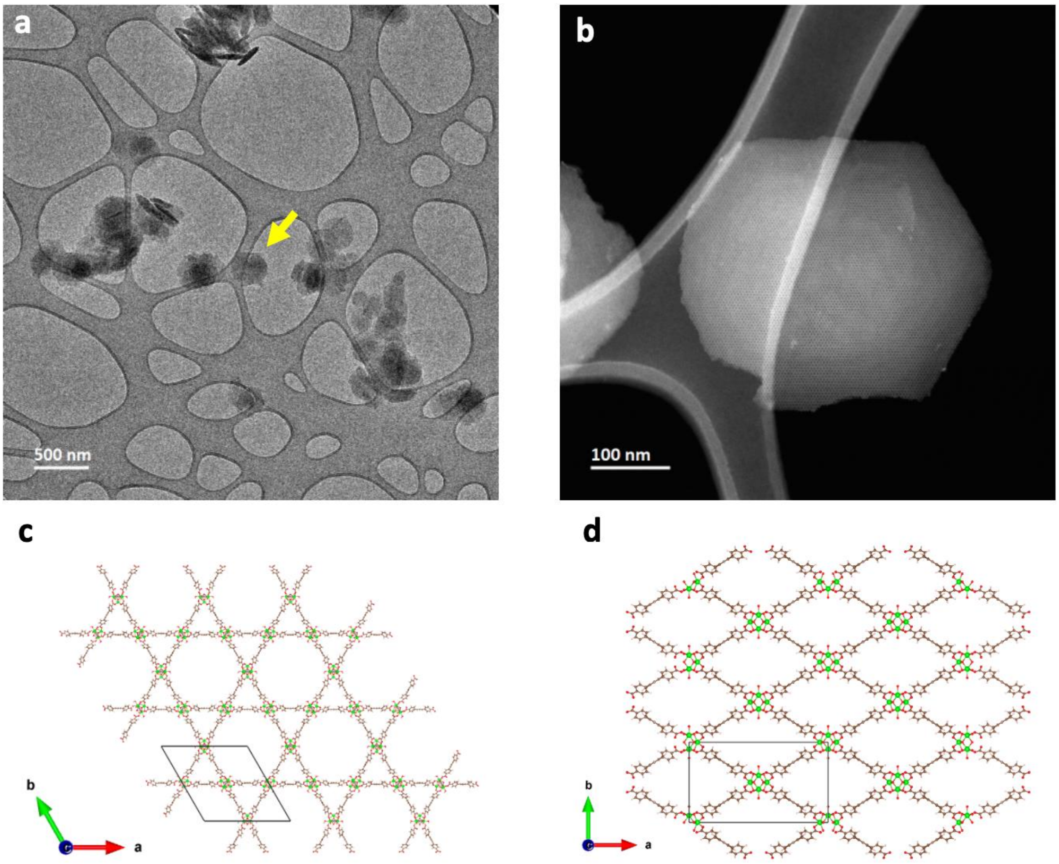

Supplementary Fig. 10. **(a)** Low-magnification TEM image and **(b)** HAADF-STEM image of the MOSS-6 crystal from which 4D-STEM datasets were acquired. **(c-d)** Structural models of NU-1000 **(c)** and NU-901 **(d)**, both viewed along the [001] zone axis.

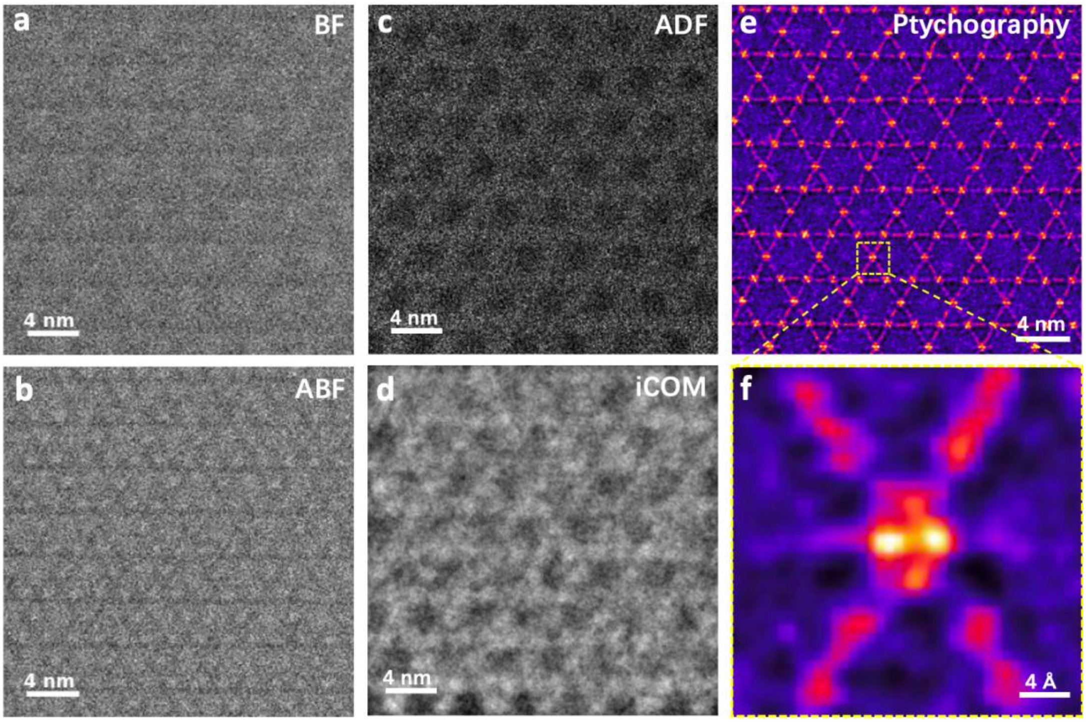

Supplementary Fig. 11. Comparison of images derived from the same 4D-STEM dataset for MOSS-6 using various imaging mechanisms: (**a**) Bright-field (BF), (**b**) annular bright-field (ABF), (**c**) annular dark-field (ADF), (**d**) integrated center-of-mass (iCOM), and (**e**) LSQ-ML-based ptychography. (**f**) Enlarged view of the square-marked area in (**e**).

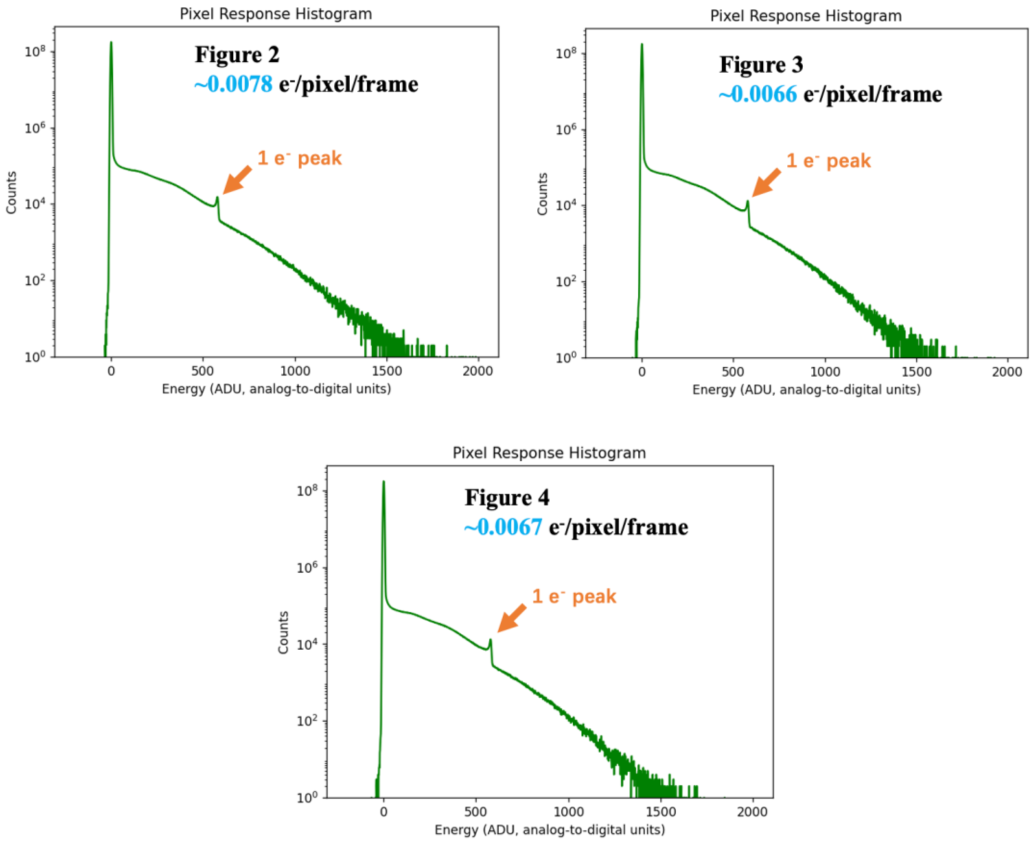

Supplementary Fig. 12. Pixel response histograms from 256×256 frames, each 128×128 pixels, in low-dose experiments. The peak at 0 ADU (analog-to-digital units) corresponds to pixels with no electrons, and the peak at approximately 580 ADU corresponds to pixels with one electron at 300 kV. No peaks for events with two or more electrons are discernible.

Supplementary Table. 2 Statistics for the 4D-STEM datasets used in Figs. 2-4.

Total pixel number: 256 * 256 * 128 * 128 = 1, 073, 741, 824			
Experimental Cases	**Figure 2: Zr-BTB**	**Figure 3: MOSS-6**	**Figure 4: MOSS-6**
Mean Illumination Intensity (e^-/pixel/frame)	~0.0078	~0.0066	~0.0067
Dose ($e^-/Å^2$)	115.47	98.40	98.88
Number of pixels receiving > 1 e^- (proportion)	562, 438 (0.052 %)	416, 334 (0.039 %)	418, 549 (0.039 %)
Number of pixels receiving > 2 e^- (proportion)	5, 023 (0.0 %)	2, 868 (0.0 %)	2624 (0.0 %)
Number of pixels receiving > 3 e^- (proportion)	30 (0.0 %)	17 (0.0 %)	1 (0.0 %)
Number of pixels receiving > 4 e^- (proportion)	0 (0.0 %)	1 (0.0 %)	0 (0.0 %)

Supplementary PDB File Proposed structural model for the intergrowth of two MOFs, NU-1000 and NU-901.